3602–3611 *Nucleic Acids Research, 2007, Vol. 35, No. 11* *Published online 7 May 2007*
doi:10.1093/nar/gkm246

Dynamics of filamentous viral RNPs prior to egress

Philip J. Santangelo* and Gang Bao*

Wallace H. Coulter Department of Biomedical Engineering, Georgia Institute of Technology and Emory University, 313 Ferst Drive, Atlanta, GA 30332, USA

Received December 31, 2006; Revised April 2, 2007; Accepted April 3, 2007

ABSTRACT

The final step in the maturation of paramyxoviruses, orthomyxoviruses and viruses of several other families, entails the budding of the viral nucleocapsid through the plasma membrane of the host cell. Many medically important viruses, such as influenza, parainfluenza, respiratory syncytial virus (RSV) and Ebola, can form filamentous particles when budding. Although filamentous virions have been previously studied, details of how viral filaments bud from the plasma membrane remain largely unknown. Using molecular beacon (MB)-fluorescent probes to image the viral genomic RNA (vRNA) of human RSV (hRSV) in live Vero cells, the dynamics of assembled viral filaments was observed to consist of three primary types of motion prior to egress from the plasma membrane: (i) filament projection and rotation, (ii) migration and (iii) non-directed motion. In addition, from information gained by imaging the 3D distribution of cellular vRNA, observing and characterizing vRNA dynamics, imaging vRNA/Myosin Va colocalization, and studying the effects of cytochalasin D (actin depolymerizing agent) exposure, a model for filamentous virion egress is presented.

INTRODUCTION

Several medically important enveloped viruses that infect the respiratory tract, such as influenza (1–3), respiratory syncytial virus (RSV) (4–8), and parainfluenza (9) virus, form both spherical and filamentous virions at the surface of infected cells. This has been observed both in cell culture models with high passage, laboratory strains, and from virus isolated directly from nasopharyngeal secretions or observed in pathology samples (7). It has been shown that in influenza, filamentous virions have a higher specific infectivity (2), and it has been theorized that the filamentous virus morphology may be more effective for both infecting cells and evading the host immune responses, particularly in the respiratory tract (3).

One important question about the filamentous virion is: What are the mechanisms by which these virions bud from the plasma membrane of an infected cell? To answer this question, we chose as our model system the A2 strain of human respiratory syncytial virus (hRSV), grown in non-polarized Vero cells. Since many aspects of virion assembly and replication have been studied with RSV, this system is ideal for the study of filamentous virion egress. To image the live-cell dynamics of the genomic viral ribonucleoprotein (vRNP) of hRSV, a molecular beacon (MB)-fluorescent probe was designed to target specifically the vRNA. This allowed for direct observations of both the morphology and mechanics of the processes leading to viral egress within the cellular context. This approach has significant advantages over the DIC (differential interference contrast) method used in the previous dynamics study (10) of RSV, which lacked molecular specificity and the contrast needed to observe vertically oriented virions.

Molecular beacons are dual-labeled, nucleic acid probes with a reporter fluorophore at one end and a quencher at the other. They are designed to form a stem-loop hairpin structure so that fluorescence emission occurs only when the probe hybridizes to a complementary target, resulting in a high signal-to-background ratio (SBR) (11). Although MBs have been used in limited live-cell mRNA studies (12–16), their potential for the analysis of viral RNA in living cells has only recently been demonstrated (17,18). Other methods for imaging RNA in live cells, including the use of fluorescently labeled full-length RNAs or RNPs (19–22) and GFP-fused RNA-binding proteins (GFP-MS2) (23), do not allow for the evaluation of unmodified viral particles.

For the imaging experiments, a single chimeric MB, with a DNA backbone stem and 2′-O-Methyl RNA backbone hybridization domain, was designed to target a gene-end-intergenic-gene-start sequence, 3′-UUU UUA CCC CGU UUA U-5′, that has three exact repeats (Figure 1A) (24,25). Successfully used in antisense experiments (24,25), this site was considered the most accessible and therefore a prime site for probe hybridization. Targeting the repeated sequence provided signal amplification, resulting in a significantly increased SBR. In addition, since the target RNP is concentrated in

*To whom correspondence should be addressed. Email: philip.santangelo@bme.gatech.edu; gang.bao@bme.gatech.edu

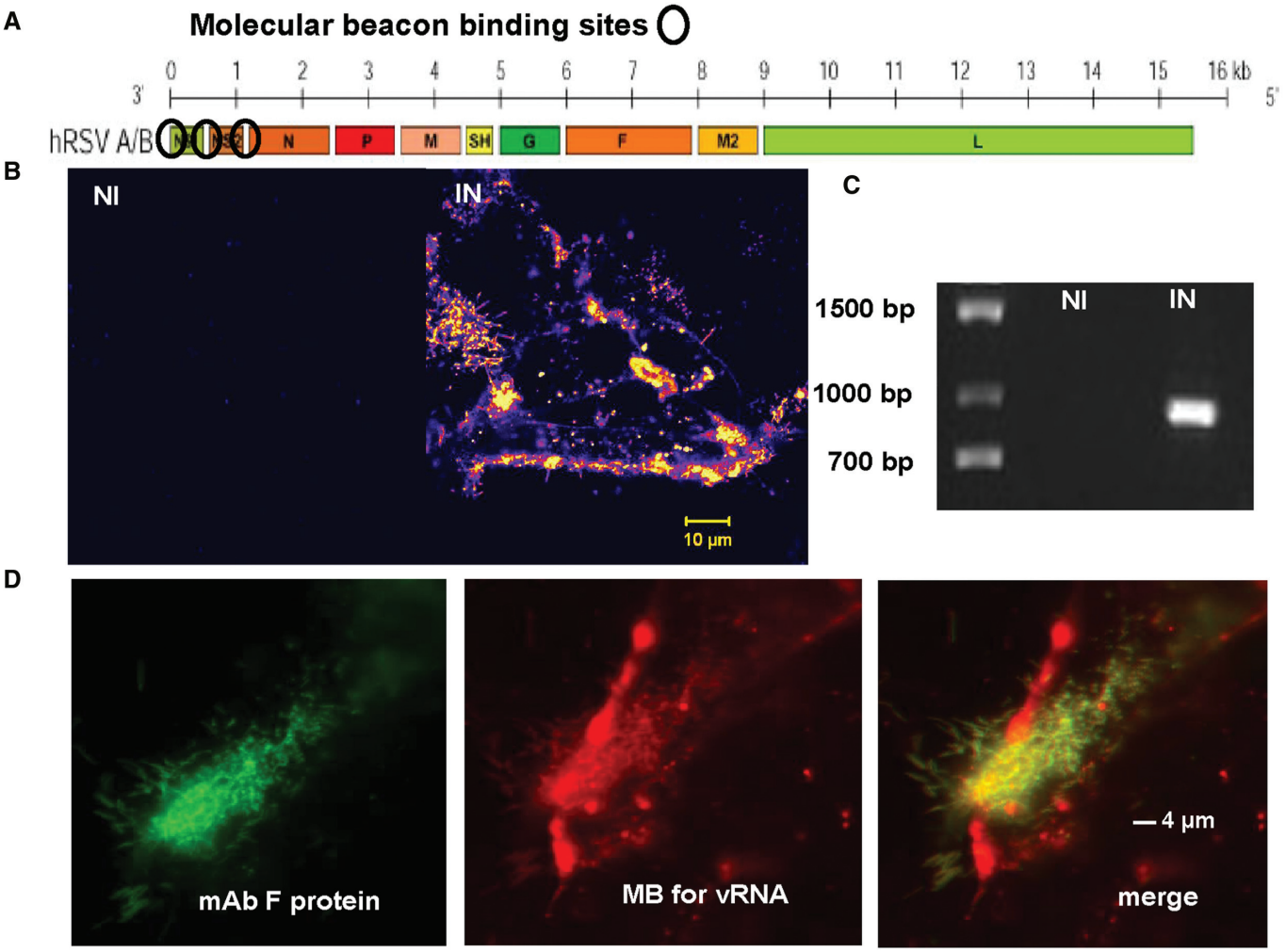

Figure 1. Characterization of the vRNPs of hRSV in live cells using molecular beacon imaging. (**A**) A schematic showing the genomic organization of hRSV with black ellipses indicating the sequence locations where the molecular beacon probe was targeted. (**B**) Image of non-infected (NI) and 2-day post-infection (IN) Vero cells, 30 min after MBs targeting the genomic vRNA of hRSV were delivered into them; infected cells exhibit highly localized signal in both inclusion bodies (aggregates of vRNA) and groups of filamentous vRNPs. (**C**) PCR results from non-infected (NI) and infected (IN) cells 2-day post-infection; no product was formed for the NI case, while the IN case showed a strong PCR product at 940 bp. (**D**) Results from live-cell delivery and hybridization of Quasar570-labeled MB to vRNA in infected cells, together with fixation and antibody staining (Alexa488) for hRSV F protein, indicating that molecular beacons could hybridize to vRNPs when they are being packaged for egress.

cytoplasmic granules, often called inclusion bodies, and in viral filaments, which contain multiple copies of the vRNP, the signal was further enhanced. A 2′-O-Methyl RNA/DNA chimera design was used for the MB primarily because of its generally higher SBR (26) when binding to RNA. This enhanced our ability to observe viral RNA being packaged into filamentous virion (SBR ranging from 11 to 30 using chimera versus less than 5 using DNA), and is likely due to 2′-O-Methyl RNAs higher affinity for RNA than DNA (27–29). The enhanced nuclease resistance is also a positive feature of using 2′-O-Methyl RNA for the hybridization domain (28), but we did not ever observe evidence of active probe degradation with DNA or chimera probes. The lack of probe degradation is likely due to the use of streptolysin O-based delivery, which avoids the endocytic pathway (12).

MATERIALS AND METHODS

Cells and virus

Vero cells (ATCC CCL-81) were grown in DMEM (Sigma Aldrich, St. Louis, MO) with 10% FBS (ATCC) with 100 U/ml of penicillin and 100 mg/ml of streptomycin. Virus used was the A2 strain of RSV (ATCC VR-1544) at a titer of 1×10^6 $TCID_{50}$/ml. The titer was evaluated by serial dilution and immunostaining, 4-days post-infection (PI). All data shown was at day 2 PI and with a multiplicity of infection (MOI) of 0.5. At 48 h numerous synctia had formed, but no cell death had occurred. All cells were infected at 80–90% confluence, by removing the media, followed by washing with 1× PBS (without Ca^{+} and Mg^{+2}), and then adding virus to the cells for 30 min at 37°C. After the 30-min incubation, regular media were added.

Molecular beacon synthesis and characterization

The MB used in this study was a DNA/2′-O-Methyl RNA chimera, 5′-Quasar570-ctcgacg AAAAAUGGGGCAA AUA cgtcgag–BHQ2 -3′ (Biosearch Technologies, Novato, CA) where the underlined sequences represent the MB stem, lower case are DNA, and the upper case are 2′-O-Methyl RNA. The beacon's SBR ratio in solution (beacon to target ratio was 1:2 in 1× PBS buffer) was measured to be ~50 using a Tecan Safire fluorescent platereader.

Live-cell molecular beacon delivery

Molecular beacons were delivered into infected and uninfected live, Vero cells on day 2 PI using a reversible permeabilization method with streptolysin O (SLO) (Sigma). Cells grown in normal medium were first washed with serum-free medium and then incubated with a mixture of 0.2 U/ml of SLO and 1 μM of MB in an appropriate amount of serum-free medium for 10 min at 37°C. The SLO/MB/serum-free medium was then removed and replaced with fresh, normal medium. For live-cell imaging, the cells were imaged via epifluorescence microscopy, 20 min after incubation in normal growth medium. Using SLO-based delivery, MBs were delivered into Vero cells with ~100% efficiency.

PCR primers and conditions

Total RNA was isolated from infected and non-infected Vero cells, day 2 PI using the Qiagen RNeasy Mini Plus kit, as per the manufacturers instructions. Reverse transcription was performed using the Thermoscript reverse transcriptase with typical conditions. Primers called BC6: 5′-TAA TTT TCA GGC TCC ATC TG-3′, and OD1: 5′-TGT TTG ACA ATG ATG AAG TA–3′ were used to amplify the gene end-intergenic-gene start region between the viral genes NS1 and NS2 (25). The cycle conditions were as follows: stage 1: 95°C 5 min 1×; stage 2: 95°C 30 s; 58°C for 45 s; 72°C 90 s stage 3: 72°C 10 min 1×, using the Invitrogen Thermoscript RT-PCR system with Platinum Taq DNA Polymerase.

Simultaneous labeling

In order to verify MB hybridization to vRNA during virion assembly, Vero cells, 2-day PI, were simultaneously labeled with both MBs for the vRNA of hRSV and with a monoclonal antibody (mAb) (Abcam RSV3206) for the hRSV F protein. Infected cells were live-cell labeled with the hRSV specific MB as discussed above. Thirty minutes after live-cell MB hybridization, cells were fixed with room temperature (RT) 4% paraformaldehyde (Electron Microscopy Sciences, Hatfield, PA) in nuclease free PBS for 10 min. They were then washed twice with 1× PBS and incubated in 5% RNase-free BSA (Fisher Scientific, Horsham, PA) in 1× PBS for 60 min at RT. They were then washed twice with 1× PBS and incubated with a 1:500 dilution of mAb RSV3206 (Abcam, Cambridge, MA) for 60 min at RT. After being washed twice with 1× PBS for 5 min, the cells were then incubated with a 1:400 dilution of Alexa 488-goat-anti-mouse IgG secondary antibody (Invitrogen, Carlsbad, CA). Cells were then washed twice with 1× PBS, mounted in Zymed clearmount and imaged.

This procedure was repeated when labeling vRNA and lipid rafts, except 30 min after live-cell MB hybridization, the Vybrant Lipid Raft Labeling Kit from Invitrogen was used as per the manufacturers' instructions on the live cells, fixed with 4% paraformaldehyde, and then imaged. For staining vRNA and myosin Va, the vRNA was labeled in live-cells with the MB as mentioned above, fixed as mentioned above, but in addition were permeabilized 0.1% Triton X in 1× PBS for 3 min, followed by a 1× PBS wash after fixation. The primary antibody used was a rabbit polyclonal to myosin Va (Santa Cruz Biotech, Santa Cruz, CA) at a 1:100 dilution in PBS; the secondary antibody used was an Alexa 488-goat-anti-rabbit IgG (Invitrogen).

Cytochalasin D treatment

In order to further understand the role of actin in the dynamics of viral genomic RNPs, MBs were delivered into Vero cells 2-day PI. Thirty minutes after MB delivery the cell media were removed and replaced with their normal growth media with 3 μg/ml of cytochalasin-D bodipy FL (Invitrogen). Time-lapse epifluorescence imaging of the cells was performed at 37°C and 5% CO2, immediately after the media were changed for ~15 min. Out of focus light was removed using ImageJ 'background subtraction' in order to improve the contrast of the filaments shown. No other alterations were performed.

3D reconstructions

Fixed cell images (in 4% paraformaldehyde in 1× PBS) of vRNPs or vRNP/myosin Va co-stained samples were imaged using a Zeiss LSM 510 Meta confocal microscope with a 100X Plan-Neofluor objective (NA = 1.3). The pinhole for the confocal microscopy was set such that each image is 0.5 μm thick, with 0.5 μm between images, and up to 31 images (~15 μm in the z direction) were taken. Bitplane was utilized to reconstruct the z-stack images. This enabled the actual length of the vRNPs to be measured, not just the 2D projection length.

Live-cell imaging

All of the live-cell imaging performed was with a Zeiss Axiovert 200 epifluorescence microscope equipped with an internal shutter, and a Zeiss Axiocam MRm cooled CCD camera. Control of the internal shutter and image acquisition was performed using Zeiss Axiovision 4.4. Chroma filter sets 41007a and 49002 were used to image the Quasar570 and Alexa 488 fluorescence, respectively. All images were taken with a 100X EC-Plan-Neofluor objective (NA = 1.3). Fixed cell imaging was performed in 4-well, Nunc Labtek II chambered coverslips (#1.5), while all live-cell imaging was performed with Bioptechs DeltaT black dishes with a #1.5 coverslip for a bottom. The live cells were kept at 37°C using the Bioptechs DeltaT4 system and objective heater, and in a 5% CO_2 in air environments via a port in the heated lid of the DeltaT4 system.

Image analysis was performed using ImageJ (NIH) v. 1.33u, or using Bitplane by Imaris. ImageJ was utilized to produce the image sequence data from the time-lapse images of vRNP dynamics, and to false color the images. The only modification to the time-lapse images was the mapping of the 8-bit gray scale to the 'fire' color maps in ImageJ. No other changes to the images were performed. SBR measurements were performed with the background intensities of both the non-infected and infected cells being the same value. Only linear changes were made to equilibrate their backgrounds. In addition, ImageJ and Bitplane were used to analyze the motion of vRNPs and the length of filamentous vRNPs. This information was then used in Microsoft Excel to calculate the mean square displacement (MSD) of the vRNPs as a function of time, and the filament length distribution.

RESULTS

Molecular beacons were delivered into a confluent monolayer of Vero cells 2-day PI with the A2 strain of hRSV, as well as non-infected Vero cells, using reversible cell membrane permeabilization with streptolysin O (12), in order to determine both the specificity of the MB probe (17) and characterize the morphologies of the vRNPs. As seen in Figure 1B, infected cells exhibited strong fluorescence with signal concentrated in spherical inclusion bodies (average SBR of 80) and individual viral filaments (average SBR of 11), while the non-infected cells were quite dark, demonstrating excellent probe specificity. The infection was confirmed using PCR; infected cells exhibited a very high level of hRSV amplicon, unlike the non-infected cells (Figure 1C). To demonstrate probe accessibility for vRNPs that were in the process of being packaged, we fixed the hRSV-infected cells after delivering MBs, and then co-stained for the RSV F protein with indirect immunofluorescence. The F or fusion protein is a membrane glycoprotein that mediates viral fusion and entry, and also promotes fusion of the infected cell membrane with adjacent cell membranes, leading to the formation of syncytia. We observed significant image overlap of the filamentous MB signal with that from the anti-F-protein antibody on the surface of the cells, indicating that MBs can bind to vRNPs localized to the inside of the plasma membrane in the midst of the packaging process (Figure 1D). In addition, the F protein and MB signal colocalization implies that the RNPs are located throughout the filament.

In order to better describe the morphologies observed using MB imaging in the infected cells, 30 min after MB delivery, the cells were fixed, imaged with confocal microscopy and later reconstructed in three dimensions using Imaris Bitplane. In Figure 2A, four images showing only the fluorescent information at distances greater than 12, 8, 4 and 0 μm from the glass surface are shown. The 0 μm view represents all of the signal from the bound MBs within the infected cells displayed in two dimensions; the cross section is ~15 μm thick from the coverglass to the tops of the viral filaments (as represented by the fluorescent signal). Both cytoplasmic inclusions and viral

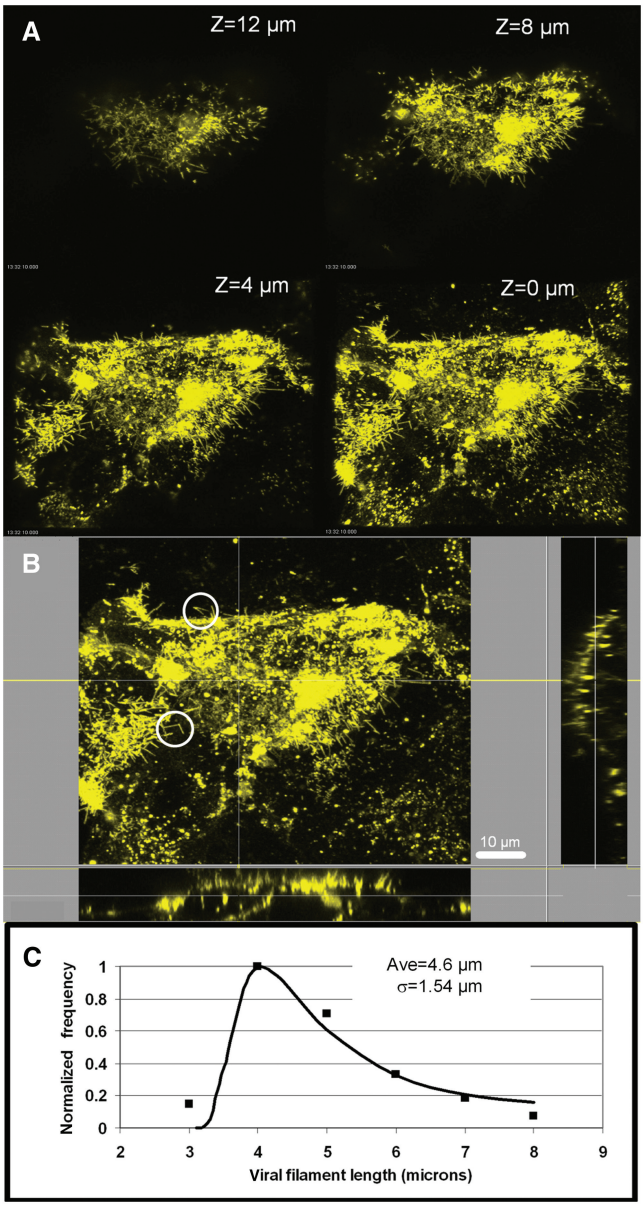

Figure 2. Two-dimensional representations of viral RNPs imaged via MB hybridization. (**A**) Four images showing only the fluorescent information at distances greater than 12, 8, 4 and 0 μm, from the glass surface. The cross section is ~15 μm thick from the coverglass to the tops of the filaments. Both cytoplasmic inclusions and viral filaments are easily viewed and measured, with the upper 3 μm (perpendicular to the image plane) dominated by filaments. (**B**) *XZ* and *YZ* cross sections are shown; the filaments are easily seen protruding from the curved, apical side of the cells, while the inclusions are distributed throughout the cytoplasm, but often closer to the apical membrane than the coverslip. Two examples of connected filaments are indicated by the white circles. (**C**) Plot of filament length distribution.

filaments are easily viewed and measured, with the upper 3 μm (perpendicular to the image plane) dominated by filaments. In Figure 2B, one *XZ* and *YZ* cross section are shown. In these cross-sectional views, the filaments are easily seen protruding from the curved, apical side of the cells, while the inclusions are distributed throughout the cytoplasm, but often closer to the apical membrane

than the coverslip. The filament lengths from the 3D reconstructions were measured in Bitplane, and the distribution is plotted in Figure 2C. The distribution is log-normal, ranging from ~2.6 to 8.1 μm, with an average filament length of 4.6 μm and a SD of 1.54 μm. This is very consistent with prior measurements of filament length measured using electron microscopy; Armstrong *et al.* (4) quoted lengths up to 2.5 μm, Norrby *et al.* (8) greater than 2 μm, Bachi and Howe (5) up to 10 μm, Berthiaume *et al.* (6) up to 5 μm, and measurements by Roberts *et al.* (7) quoted a range from 4 to 8 μm. In addition, we found that some filamentous vRNPs (Figure 2B, white circles) are connected at one end, with average angles of $\sim 71.4 \pm 3.5^{\circ}$, which is very similar to morphologies formed by the actin network near the plasma membrane (30,31).

Time-lapse imaging experiments were performed on Vero cells, 2-day PI, in order to observe the dynamics leading to virion egress. Images of infected cells were taken using 100–200 ms exposures, with 5 s between exposures for up to 15 min, after which photobleaching became significant. Twelve image sequences were taken per experiment and 10 experiments were performed, yielding 120 time-lapse movies. After analyzing the movie sequences, three primary modes of motion were identified: (i) filament projection and rotation, (ii) migration, and (iii) non-directed motion. As shown in Figure 3A and Supplementary Movie 1, filamentous vRNPs on the surface of the cells rotated dramatically on one end after a period of little motion. A quantitative analysis indicated that the vRNPs in Figure 3A exhibited little rotation for ~250 s, then rapidly rotated to a near vertical position relative to the cell membrane within 50 s (Figure 3B). The average rate of rotation after the vRNPs appeared to separate from the membrane was $\sim 1.67^{\circ}$/s. Once the vRNPs became vertical, they either continued to rotate rapidly (Figure 3C and Supplementary Movie 2), with a rate $\leq 6^{\circ}$/s, or they migrated over short distances, exhibiting the second mode of motion observed (migration). It should be noted that the filamentous groups of vRNPs observed while rotating are flexible in nature. An example of a flexible filament can be observed in Figure 3D, panel two (5 s, where the filament appears 'bent'), and panel three (10 s, where the filament appears curved) and in Supplementary Movie 2. The flexibility of RSV nucleocapsids has previously been noted (32), but were not observed in real-time during the egress process.

A typical example of the migration mode can be seen in Figure 4A and Supplementary Movie 3, where a vertically oriented vRNP migrated ~2.8 μm in 50 s; the path of the vRNP is plotted in Figure 4B. Prior to and after this migration, the particle is static. The path taken by the particle is very similar in morphology to that of lipid rafts (see inset in Figure 4B) as imaged using an Alexa 488-labeled cholera toxin probe. We hypothesize that the raft acts as a guide for the particle path, which is consistent with the observation that vRNP packaging occurs in the lipid rafts (33–36). The speeds observed of ~25 migrating filaments ranged from ~29.5 to 102 nm/s with an average speed of 56 nm/s, while the path lengths traveled ranged from ~1 to 4 μm, with an average path length of 2.36 ± 0.9 μm. The speeds measured are commensurate with myosin transport (37); myosin has been implicated in RSV viral protein trafficking (38) and given the connection between lipid rafts and the actin network (39), myosin-driven transport likely plays a role in RSV virion egress.

In addition, many vRNPs exhibited non-directed motion over periods greater than 15 min, as illustrated in Figure 4C and Supplementary Movie 4 (A control video, where MBs were delivered into non-infected Vero cells, can be seen in Supplementary Movie 5). In order to compare the motion seen in Figure 4A with that observed in 4C, and gain insight into the nature of the motion, the MSD or $\langle r^2 \rangle$ of each trajectory was calculated (Figure 4D). It was determined that for the motion in Figure 4A, the MSD (Figure 4D), could be fit by a parabola ($[\langle r^2 \rangle = 4Dt + (vt)^2]$, where $D = 0.0033\ \mu m^2/s$, and $v = 29.05$ nm/s, with an $R^2 = 0.984$, representing directed motion; while the motion in Figure 4C could be fit ($R^2 = 0.7$) by a power law function $\langle r^2 \rangle = 4Dt^{\alpha}$, where $4D = 0.013$ and $\alpha = 0.78$ ($R^2 = 0.7$), which is between $0.5 < \alpha < 0.9$ representing anomalous diffusion or obstructed diffusion (22,40,41). The calculations shown in Figure 4D are for the particles shown, but are representative of the populations exhibiting these modes of motion. In Figure 4E, the fraction of filaments exhibiting each mode of motion is presented. Approximately 36% exhibit projection and rotation, 12% migration and 52% non-directed motion.

DISCUSSION

Role of actin and myosin

In the previous section, evidence of the directed motion of the RSV filamentous vRNPs was presented. This evidence, in conjunction with previous studies of RSV filaments (34–36,42–46), points to motor driven transport on the cytoskeleton as the likely driver of the observed migratory motion, and possibly the rotational motion. Previous studies of RSV have demonstrated that actin filaments (42,46) and their growth, mediated by profilin (43) and rhoA activation (44), are vital to virion egress. In many of those studies, infected cells were exposed to cytoskeletal depolymerizing agents. The amount of free virion or viral RNA in the cell culture media, or changes in virion morphology, as measured via immunofluorescence imaging, were used to gauge the effect of these agents on virion egress. In previous studies, actin depolymerization via cytochalasin D had the most adverse effects on virion egress, therefore making actin/myosin the most likely cytoskeletal/motor combination involved in the motion observed in our investigation. In addition, since assembly occurs at the lipid rafts and the rafts are linked to the actin network (39), depolymerzing them should effect the observed motion.

Live-cell MB hybridization, cell fixation and permeabilization, followed by immunostaining of myosin Va, and confocal microscopy imaging was performed in order to confirm the presence and possible role of myosin. Myosin V has previously been implicated in trafficking messenger RNP (47), granules on the actin network near

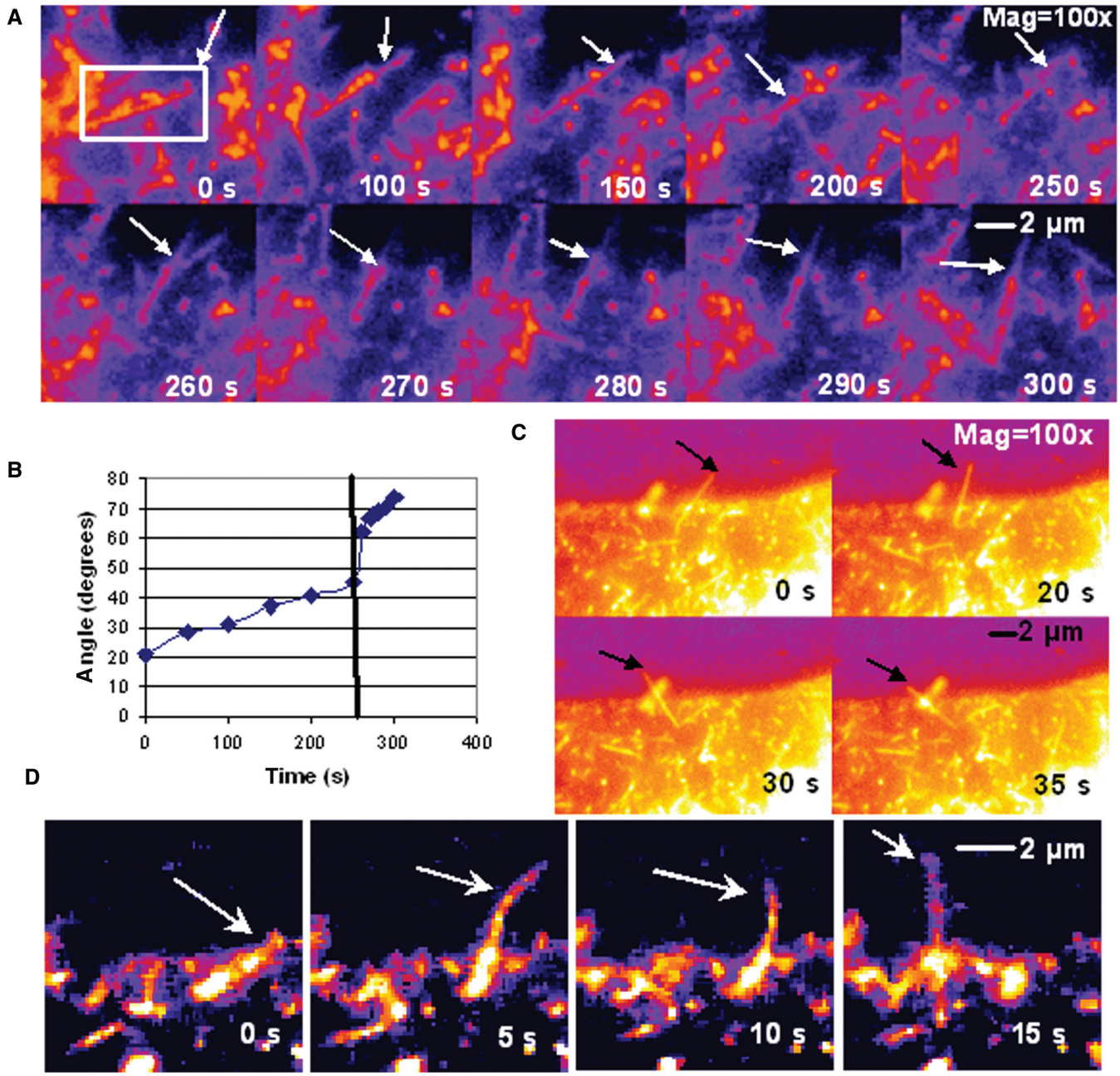

Figure 3. Time-lapse fluorescent imaging of the rotational dynamics of hRSV filamentous vRNPs. (**A**) Time series of the dynamics of vRNPs (white box), exhibiting the projection and rotation mode of motion. (**B**) Quantification of rotation angle; after 250 s of very limited motion, the virion rapidly rotates to near vertical (represented by the vertical black line), possibly separating much of it from the plasma membrane. The angle measurement was made relative to the vRNPs initial position at the cell membrane. The initial position was confirmed via fluorescence imaging to be at the cell membrane, via the vRNPs colocalization with the lipid rafts (data not shown). (**C**) Once the vRNPs are vertical, two types of motion were observed, violent rotation (see Supplementary Movie 2) or migration. A time series of the rapid rotation of packaged vRNPs is shown here; where within 15 s, the vRNPs pictured here rotate 69.4°. (**D**) The flexibility of RSV filaments is shown in this time-lapse sequence. The RSV filament appears both 'bent' and exhibits curvature at both 5 and 10 s from the initial time of observation.

the plasma membrane (48), and RSV proteins to the apical membrane in polarized cells (38). The results from our simultaneous labeling experiments can be seen in Figure 5, where the blue represents myosin Va, the red represents vRNPs (hybridized MBs) and the purple represents their colocalization. In Figure 5A, like Figure 2A, four images showing only the fluorescence information at distances greater than 9, 6, 3 and 0 μm from the glass surface are shown. The 0 μm view represents all of the fluorescent signal from within the infected cells, displayed in two dimensions; the cross section is ~12 μm thick from the coverglass to the tops of the viral filaments. In Figure 5B, *XZ* and *YZ* cross-sectional views are shown, with crossed lines representing where they were taken in the *XY* plane.

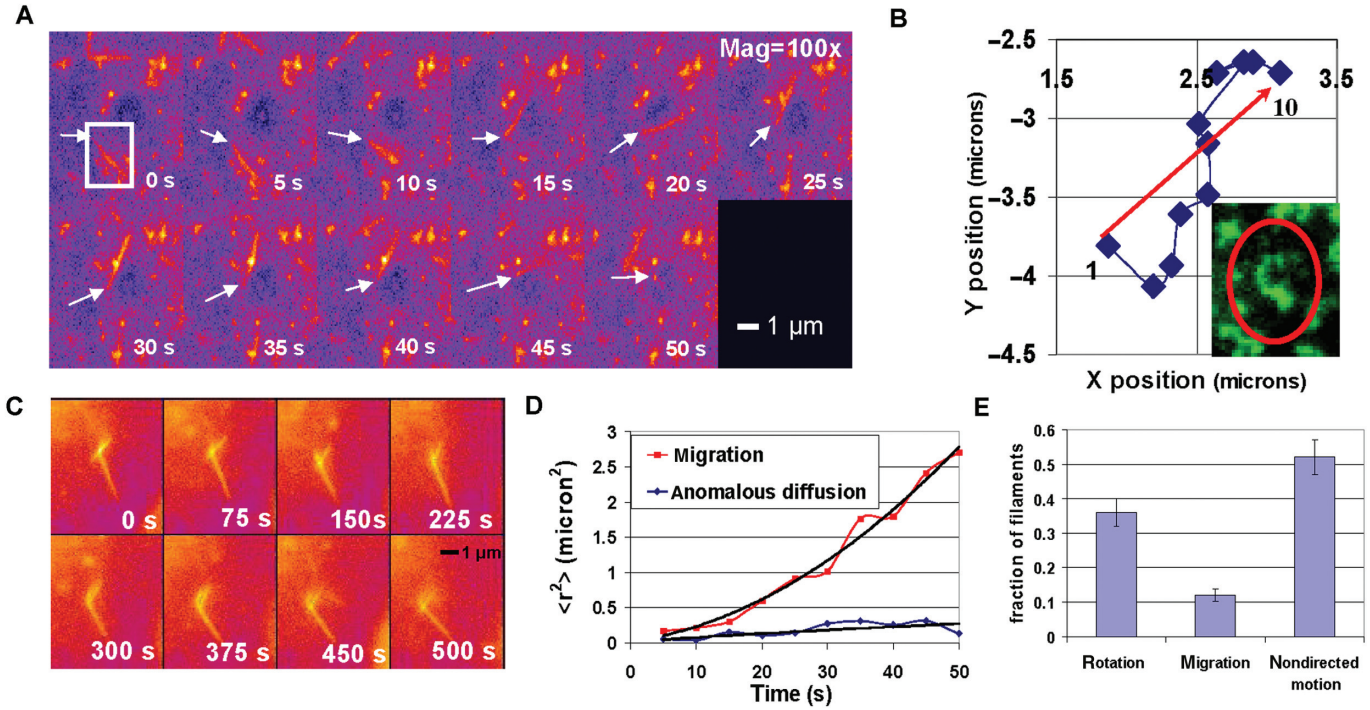

Figure 4. Migration and diffusion dynamics of hRSV filamentous vRNPs. (**A**) A time series of the dynamics of vRNPs (white box), exhibiting migration. (**B**) The trajectory of migration (from the point labeled 1 and ending with the point labeled 10) is shown in (B). The shape of the trajectory shown in (B), is very similar to the shape of the lipid rafts of Vero cells, as can be seen in the inset image, with a typical raft (~1.2 µm in length) circled in red. (**C**) A time series of vRNPs exhibiting non-directed motion or anomalous diffusion is shown. (**D**) Plot of the mean square displacement (MSD) or $\langle r^2 \rangle$ of trajectories presented in (A) and (C). The MSD of (A) was fit with a parabola, representing directed motion; while for the motion in (C) could be fit by a power law fit with an exponential value between 0.5 and 0.9 representing anomalous diffusion or obstructed diffusion. (**E**) Plot of the relative fraction of filaments exhibiting each of the three types of motion observed.

From the data in Figure 5A and B, it can be seen that the filaments are largely distributed along the apical surface, and that they colocalize well with myosin Va (purple color). Throughout the volume of the cell monolayer, both myosin Va (blue), represented as small dots, and vRNPs (MB, red), predominately in cytoplasmic inclusions, do not colocalize and appear independent. It is clear from this figure that the strongest colocalization occurs predominately in the filaments and near the surface of the monolayer, implicating myosin Va's role in the assembly and egress process.

Vero cells 2-day PI and hybridized with RSV targeted MBs, were exposed to cytochalasin D, an actin depolymerising agent, in order to provide further evidence for the role of actin on the vRNP morphology and dynamics. We observed that many filamentous vRNPs exposed to cytochalasin D, tended to aggregate and form circular, inclusion-like structures of vRNPs within ~1 min (Figure 6A and Supplementary Movie 6). Two minutes later, these circular aggregates tended to move from the surface of the cell into the cell cytoplasm. After 15 min, almost all of the vRNPs had separated from the cell surface and were concentrated in granules. In Figure 6B, a typical syncytia is shown; high concentrations of filamentous structures surround the syncytia, while a lower density of filaments and particles lie along the apical membrane. However, as shown in Figure 6C, a syncytia 15 min after cytochalasin D exposure composed of predominately circular granules. This experiment helps confirm filamentous actin's role in governing vRNP morphology, and explain why virion egress is decreased when actin filaments are depolymerized.

From the data presented in this investigation and from previous studies, we hypothesize that actin filaments and myosin-driven motion are the root cause of the motion observed, and such motion is mechanically separating the packaged vRNPs from the actin network, thus allowing them to leave the cell.

Biophysical model of virion egress

In order to further explain the observed dynamics of filamentous vRNPs in live cells, we propose a biophysical model. Presented in Figure 7A–D are sketches of the possible actin network/nucleocapsid interactions for all three types of motion discussed above. Figure 7A and B represents how vRNP rotation might be achieved. Myosin motors, attached to the vRNP and moving along the actin network, could cause the virion to flip up on one end (Figure 3A), given that actin filaments are quite flexible. It is possible that this motion frees much of the virion from the plasma membrane, allowing for more rigorous rotation (Figure 3C) or migration (Figure 4A). The rigorous rotation may cause the separation of daughter actin strands within the virion from mother strands at the Arp2/3 interface (31,49). The dissociation

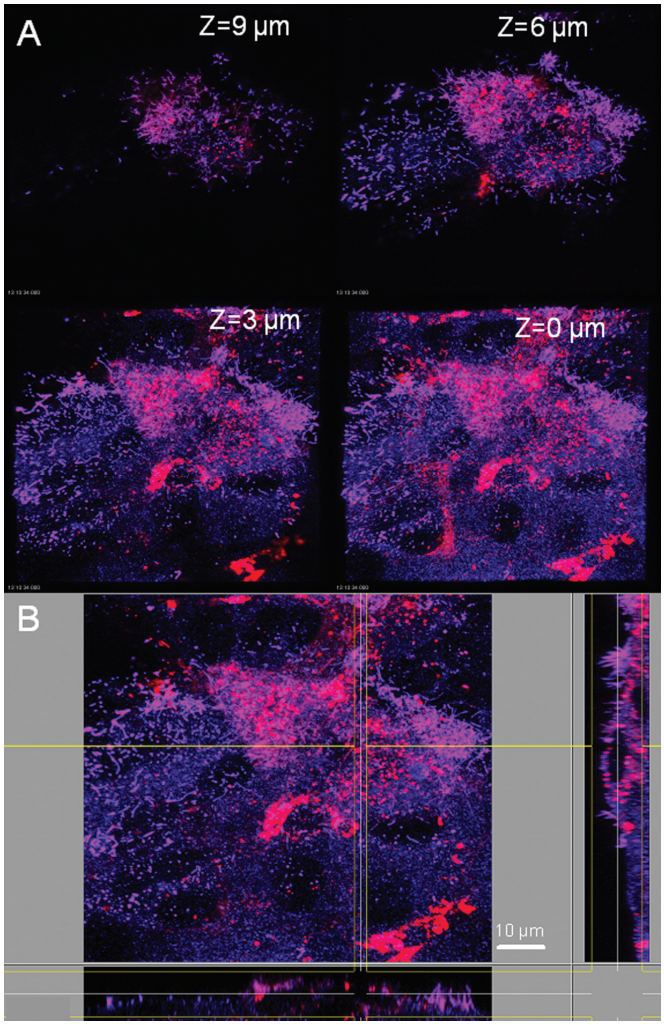

Figure 5. Simultaneous imaging of vRNPs and Myosin Va. (**A**) Four images showing only the fluorescence information at distances greater than 9, 6, 3 and 0 µm from the glass surface are shown. The cross section is 12 µm thick from the coverglass to the tops of the filaments. Myosin Va is represented in blue, vRNPs in red and the colocalization in purple. (**B**) *XZ* and *YZ* cross-sectional views. The filaments are largely distributed along the apical surface, and colocalize with myosin Va. Throughout the volume of the cell monolayer, myosin Va, small dots and vRNPs, predominately in cytoplasmic inclusions, do not colocalize and appear independent.

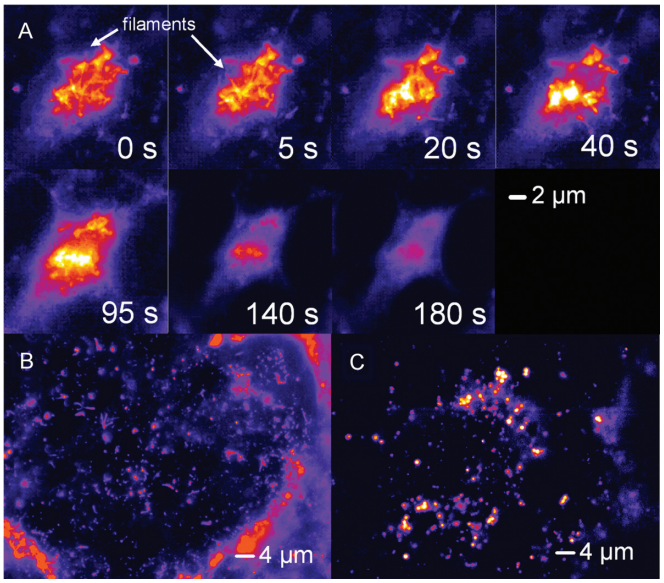

Figure 6. Actin's role in vRNP dynamics and morphology. (**A**) Seven images representing the time-lapse effects of cytochalasin D on the morphology and location of filamentous vRNPs. Initially filamentous vRNPs tended to aggregate and form circular aggregates within 1 min of exposure to media containing cytochalasin D. By 3 min, these circular aggregates, tended to move from the surface of the cell into the cell cytoplasm. (**B**) Representative example of a typical syncytia, showing high concentrations of filamentous structures around the outside of the syncytia and a lower concentration along the apical surface. (**C**) Representative image of a syncytia after cytochalasin D exposure, composed of predominately circular granules.

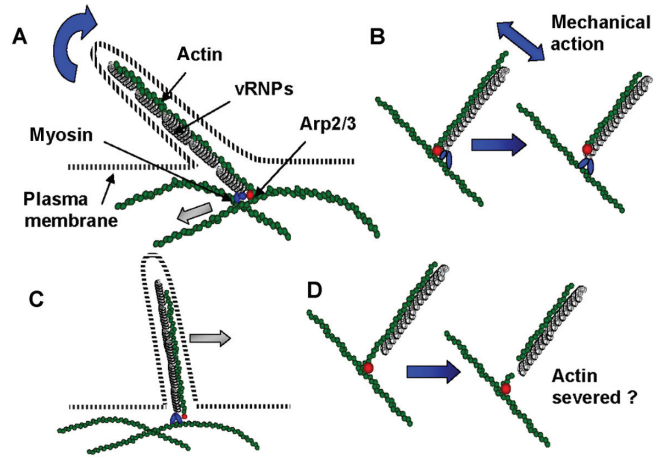

Figure 7. Hypothesized biophysical model of vRNP motion. (**A**) Active myosin V motor proteins, attached to both the viral genomic RNP and the actin network, cause the rotation of the virion and partial separation from the plasma membrane, via their translation along the actin network. (**B** and **C**) Once the virion is partially free from the cell surface due to vigorous motion (B), motor motion could possibly cause daughter actin filaments within the virion to break from the mother filaments at the Arp2/3 protein complex, allowing for rigorous rotation (Figure 3C and Supplementary Movie 2) or (C) migration along the actin network (Figure 4A and Supplementary Movie 3). (**D**) Some particles exhibit 'non-directed' or obstructed diffusion (Figure 3C and Supplementary Movie 4), possibly due to the action of the ADF/cofilin complex leaving it embedded in the membrane without the actin network/motors to propel it from the cell.

constant for Arp2/3 with the mother strand is ~50 times higher than with the daughter strand, and thus the weakest part of the structure (37). This separation would then allow the virion to leave the cell. The initiation of migration (Figure 4A) may be the result of myosin motors as a part of the virion, and their intermittent function once the vRNPs are physically separated from the actin network. This is supported by our observation of myosin Va colocalization with vRNPs (see Figure 5A and B). Non-directed motion or anomalous diffusion (Figure 4C) may occur for several reasons; for example, if vRNPs lack the ATP necessary to cause directed motion or if the vRNPs are separated from the actin network via the ADF/cofilin mechanism (31) too early and not by mechanical motion, they may be left trapped within the

plasma membrane. It is also possible that these virions were released from an infected cell earlier and reabsorbed, or they are involved in genome replication, and not competent for egress. Future studies of the protein/vRNP interactions at the membrane are required to reveal the exact reasons of the non-directed motions, and identify conclusively the proteins involved in this process.

SUPPLEMENTARY DATA

Supplementary Data are available at NAR Online.

ACKNOWLEDGEMENTS

We thank R. Compans at Emory University for his encouragement regarding the subject matter of the paper and his editorial comments, and E. Mocarski at the Emory Vaccine Center at Emory University for his editorial comments. We would also like to acknowledge NIH Grant number 1P20GM072069-01 for funding this work. Funding to pay the Open Access publication charges for this article was provided by the grant mentioned above and the Georgia Institute of Technology.

Conflict of interest statement. None declared.

REFERENCES

1. Mosley,V.M. and Wyckoff,R.W.G. (1946) Electron micrography of the virus of influenza. *Nature*, **157**, 263.
2. Ada,G.L., Perry,B.T. and Edney,M. (1957) Infectivity of influenza virus filaments. *Nature*, **180**, 1134.
3. Roberts,P.C. and Compans,R.W. (1998) Host cell dependence of viral morphology. *Proc. Natl Acad. Sci. USA*, **95**, 5746–5751.
4. Armstrong,J.A., Pereira,H.G. and Velentine,R.C. (1962) Morphology and development of respiratory syncytial virus in cell cultures. *Nature*, **196**, 1179–1181.
5. Bachi,T. and Howe,C. (1973) Morphogenesis and ultrastructure of respiratory syncytial virus. *J. Virol.*, **12**, 1173–1180.
6. Berthiaume,L., Joncas,J. and Pavilanis,V. (1974) Comparative structure, morphogenesis and biological characteristics of the respiratory syncytial (RS) virus and the pneumonia virus of mice (PVM). *Arch. Gesamte. Virusforsch.*, **45**, 39–51.
7. Roberts,S.R., Compans,R.W. and Wertz,G.W. (1995) Respiratory syncytial virus matures at the apical surfaces of polarized epithelial cells. *J. Virol.*, **69**, 2667–2673.
8. Norrby,E., Marusyk,H. and Orvell,C. (1970) Morphogenesis of respiratory syncytial virus in a green monkey kidney cell line (Vero). *J. Virol.*, **6**, 237–242.
9. Yao,Q. and Compans,R.W. (2000) Filamentous particle formation by human parainfluenza virus type 2. *J. Gen. Virol.*, **81**, 1305–1312.
10. Bachi,T. (1988) Direct observation of the budding and fusion of an enveloped virus by video microscopy of viable cells. *J. Cell Biol.*, **107**, 1689–1695.
11. Tyagi,S. and Kramer,F.R. (1996) Molecular beacons: probes that fluoresce upon hybridization. *Nat. Biotechnol.*, **14**, 303–308.
12. Santangelo,P.J., Nix,B., Tsourkas,A. and Bao,G. (2004) Dual FRET molecular beacons for mRNA detection in living cells. *Nucleic Acids Res.*, **32**, e57.
13. Tyagi,S. and Alsmadi,O. (2004) Imaging native beta-actin mRNA in motile fibroblasts. *Biophys. J.*, **87**, 4153–4162.
14. Bratu,D.P., Cha,B.J., Mhlanga,M.M., Kramer,F.R. and Tyagi,S. (2003) Visualizing the distribution and transport of mRNAs in living cells. *Proc. Natl Acad. Sci. USA*, **100**, 13308–13313.
15. Mhlanga,M.M., Vargas,D.Y., Fung,C.W., Kramer,F.R. and Tyagi,S. (2005) tRNA-linked molecular beacons for imaging mRNAs in the cytoplasm of living cells. *Nucleic Acids Res.*, **33**, 1902–1912.
16. Nitin,N., Santangelo,P.J., Kim,G., Nie,S. and Bao,G. (2004) Peptide-linked molecular beacons for efficient delivery and rapid mRNA detection in living cells. *Nucleic Acids Res.*, **32**, e58.
17. Santangelo,P., Nitin,N., LaConte,L., Woolums,A. and Bao,G. (2006) Live-cell characterization and analysis of a clinical isolate of bovine respiratory syncytial virus, using molecular beacons. *J. Virol.*, **80**, 682–688.
18. Cui,Z.Q., Zhang,Z.P., Zhang,X.E., Wen,J.K., Zhou,Y.F. and Xie,W.H. (2005) Visualizing the dynamic behavior of poliovirus plus-strand RNA in living host cells. *Nucleic Acids Res.*, **33**, 3245–3252.
19. Ainger,K., Avossa,D., Morgan,F., Hill,S.J., Barry,C., Barbarese,E. and Carson,J.H. (1993) Transport and localization of exogenous myelin basic protein mRNA microinjected into oligodendrocytes. *J. Cell Biol.*, **123**, 431–441.
20. Jacobson,M.R. and Pederson,T. (1998) Localization of signal recognition particle RNA in the nucleolus of mammalian cells. *Proc. Natl Acad. Sci. USA*, **95**, 7981–7986.
21. Tokunaga,K., Shibuya,T., Ishihama,Y., Tadakuma,H., Ide,M., Yoshida,M., Funatsu,T., Ohshima,Y. and Tani,T. (2006) Nucleocytoplasmic transport of fluorescent mRNA in living mammalian cells: nuclear mRNA export is coupled to ongoing gene transcription. *Genes Cells*, **11**, 305–317.
22. Babcock,H.P., Chen,C. and Zhuang,X. (2004) Using single-particle tracking to study nuclear trafficking of viral genes. *Biophys. J.*, **87**, 2749–2758.
23. Shav-Tal,Y., Darzacq,X., Shenoy,S.M., Fusco,D., Janicki,S.M., Spector,D.L. and Singer,R.H. (2004) Dynamics of single mRNPs in nuclei of living cells. *Science*, **304**, 1797–1800.
24. Player,M.R., Barnard,D.L. and Torrence,P.F. (1998) Potent inhibition of respiratory syncytial virus replication using a 2-5A-antisense chimera targeted to signals within the virus genomic RNA. *Proc. Natl Acad. Sci. USA*, **95**, 8874–8879.
25. Jairath,S., Vargas,P.B., Hamlin,H.A., Field,A.K. and Kilkuskie,R.E. (1997) Inhibition of respiratory syncytial virus replication by antisense oligodeoxyribonucleotides. *Antiviral. Res.*, **33**, 201–213.
26. Kehlenbach,R.H. (2003) In vitro analysis of nuclear mRNA export using molecular beacons for target detection. *Nucleic Acids Res.*, **31**, e64.
27. Majlessi,M., Nelson,N.C. and Becker,M.M. (1998) Advantages of 2′-O-methyl oligoribonucleotide probes for detecting RNA targets. *Nucleic Acids Res.*, **26**, 2224–2229.
28. Sproat,B.S., Lamond,A.I., Beijer,B., Neuner,P. and Ryder,U. (1989) Highly efficient chemical synthesis of 2′-O-methyloligoribonucleotides and tetrabiotinylated derivatives; novel probes that are resistant to degradation by RNA or DNA specific nucleases. *Nucleic Acids Res.*, **17**, 3373–3386.
29. Tsourkas,A., Behlke,M.A. and Bao,G. (2003) Hybridization of 2′-O-methyl and 2′-deoxy molecular beacons to RNA and DNA targets. *Nucleic Acids Res.*, **31**, 5168–5174.
30. Egile,C., Rouiller,I., Xu,X.P., Volkmann,N., Li,R. and Hanein,D. (2005) Mechanism of filament nucleation and branch stability revealed by the structure of the Arp2/3 complex at actin branch junctions. *PLoS Biol.*, **3**, e383.
31. Pollard,T.D. and Borisy,G.G. (2003) Cellular motility driven by assembly and disassembly of actin filaments. *Cell*, **112**, 453–465.
32. Bhella,D., Ralph,A., Murphy,L.B. and Yeo,R.P. (2002) Significant differences in nucleocapsid morphology within the Paramyxoviridae. *J. Gen. Virol.*, **83**, 1831–1839.
33. McCurdy,L.H. and Graham,B.S. (2003) Role of plasma membrane lipid microdomains in respiratory syncytial virus filament formation. *J. Virol.*, **77**, 1747–1756.
34. Brown,G., Aitken,J., Rixon,H.W. and Sugrue,R.J. (2002) Caveolin-1 is incorporated into mature respiratory syncytial virus particles during virus assembly on the surface of virus-infected cells. *J. Gen. Virol.*, **83**, 611–621.
35. Brown,G., Rixon,H.W. and Sugrue,R.J. (2002) Respiratory syncytial virus assembly occurs in GM1-rich regions of the host-cell membrane and alters the cellular

distribution of tyrosine phosphorylated caveolin-1. *J. Gen. Virol.*, **83**, 1841–1850.
36. Jeffree,C.E., Rixon,H.W., Brown,G., Aitken,J. and Sugrue,R.J. (2003) Distribution of the attachment (G) glycoprotein and GM1 within the envelope of mature respiratory syncytial virus filaments revealed using field emission scanning electron microscopy. *Virology*, **306**, 254–267.
37. Pollard,T.D. and Earnshaw,W. (2004) *Cell Biology*. updated ed. Saunders.
38. Brock,S.C., Goldenring,J.R. and Crowe,J.E.Jr (2003) Apical recycling systems regulate directional budding of respiratory syncytial virus from polarized epithelial cells. *Proc. Natl Acad. Sci. USA*, **100**, 15143–15148.
39. Lillemeier,B.F., Pfeiffer,J.R., Surviladze,Z., Wilson,B.S. and Davis,M.M. (2006) Plasma membrane-associated proteins are clustered into islands attached to the cytoskeleton. *Proc. Natl Acad. Sci. USA*, **103**, 18992–18997.
40. Bacher,C.P., Reichenzeller,M., Athale,C., Herrmann,H. and Eils,R. (2004) 4-D single particle tracking of synthetic and proteinaceous microspheres reveals preferential movement of nuclear particles along chromatin - poor tracks. *BMC Cell Biol.*, **5**, 45.
41. Seisenberger,G., Ried,M.U., Endress,T., Buning,H., Hallek,M. and Brauchle,C. (2001) Real-time single-molecule imaging of the infection pathway of an adeno-associated virus. *Science*, **294**, 1929–1932.
42. Burke,E., Dupuy,L., Wall,C. and Barik,S. (1998) Role of cellular actin in the gene expression and morphogenesis of human respiratory syncytial virus. *Virology*, **252**, 137–148.
43. Bitko,V., Oldenburg,A., Garmon,N.E. and Barik,S. (2003) Profilin is required for viral morphogenesis, syncytium formation, and cell-specific stress fiber induction by respiratory syncytial virus. *BMC Microbiol.*, **3**, 9.
44. Gower,T.L., Pastey,M.K., Peeples,M.E., Collins,P.L., McCurdy,L.H., Hart,T.K., Guth,A., Johnson,T.R. and Graham,B.S. (2005) RhoA signaling is required for respiratory syncytial virus-induced syncytium formation and filamentous virion morphology. *J. Virol.*, **79**, 5326–5336.
45. Kallewaard,N.L., Bowen,A.L. and Crowe,J.E.Jr (2005) Cooperativity of actin and microtubule elements during replication of respiratory syncytial virus. *Virology*, **331**, 73–81.
46. Ulloa,L., Serra,R., Asenjo,A. and Villanueva,N. (1998) Interactions between cellular actin and human respiratory syncytial virus (HRSV). *Virus Res.*, **53**, 13–25.
47. Jansen,R.P. (1999) RNA-cytoskeletal associations. *FASEB. J.*, **13**, 455–466.
48. Eichler,T.W., Kogel,T., Bukoreshtliev,N.V. and Gerdes,H.H. (2006) The role of myosin Va in secretory granule trafficking and exocytosis. *Biochem. Soc. Trans*, **34**, 671–674.
49. Svitkina,T.M. and Borisy,G.G. (1999) Arp2/3 complex and actin depolymerizing factor/cofilin in dendritic organization and treadmilling of actin filament array in lamellipodia. *J. Cell Biol.*, **145**, 1009–1026.